

# Performance of the MICE diagnostic systems

5

The MICE Collaboration

## Abstract

Muon beams of low emittance provide the basis for the intense, well-characterised neutrino beams of a neutrino factory and for multi-TeV lepton-antilepton collisions at a muon collider. The international Muon Ionization Cooling Experiment (MICE) has demonstrated the principle of ionization cooling, the technique by which it is proposed to reduce the phase-space volume occupied by the muon beam at such facilities. This paper documents the performance of the detectors used in the MICE experiment to measure the muon-beam parameters. The integration of the instrumentation in a comprehensive diagnostic system will also be described.

## 1 Introduction

Either a muon collider or a neutrino factory would require having high intensity and the phase-space volume occupied by the muon beam to be reduced before the injection into the storage ring [1]. Due to the lifetime of the muon, the only feasible cooling technique would be the ionisation cooling [2] where muons pass through material before being re-accelerated. The net effect would be a reduction of the transverse emittance while the longitudinal energy is restored. MICE, demonstrating for the first time this technique [3], has made the idea of those facility a concrete possibility for the future.

MICE was operated parasitically of the ISIS proton synchrotron, based at the Rutherford Appleton Laboratory (STFC). ISIS accelerates protons up to 800 MeV at a repetition rate of 50 Hz, while a titanium target is dipped nearly once per second in the outer halo of the proton beam. Pions are generated in the interaction and captured inside the MICE beamline by a set of quadrupoles and dipoles (figure 1). Pions inside the Decay Solenoid decay to muons. The transported beam initial emittance is altered before entering in the cooling channel by a set of adjustable diffusers providing further multiple scattering.

MICE was instrumented with a range of detectors used for particle identification and position-momentum measurement as described in this paper, used to fully characterise the beam and its evolution across the cooling channel.

## 30 2 Time-of-Flight Detectors

### 2.1 Introduction

Three time-of-flight detectors (TOF0, TOF1, TOF2) were built and installed at RAL in 2008 and 2009 to measure the position and the time of crossing particles. TOF0 and TOF1 [4][5][6] were placed upstream of the cooling channel, and TOF2 [7] was downstream of the channel, mounted in front of the KL, as shown in figure 1. The time of flight between two TOF stations provided particle identification information and can also be used for momentum measurement. TOF1 served most of the time also as an experimental trigger. They operated smoothly during the running periods of the MICE experiment and were essential for all the measurements done [8][9].

The good performances of the TOF detectors, over an extended period of time, enabled the MICE experiment to characterise fully its muon beams during the early stages of data-taking, by measuring their emittance [10] and assessing their pion contamination [11].

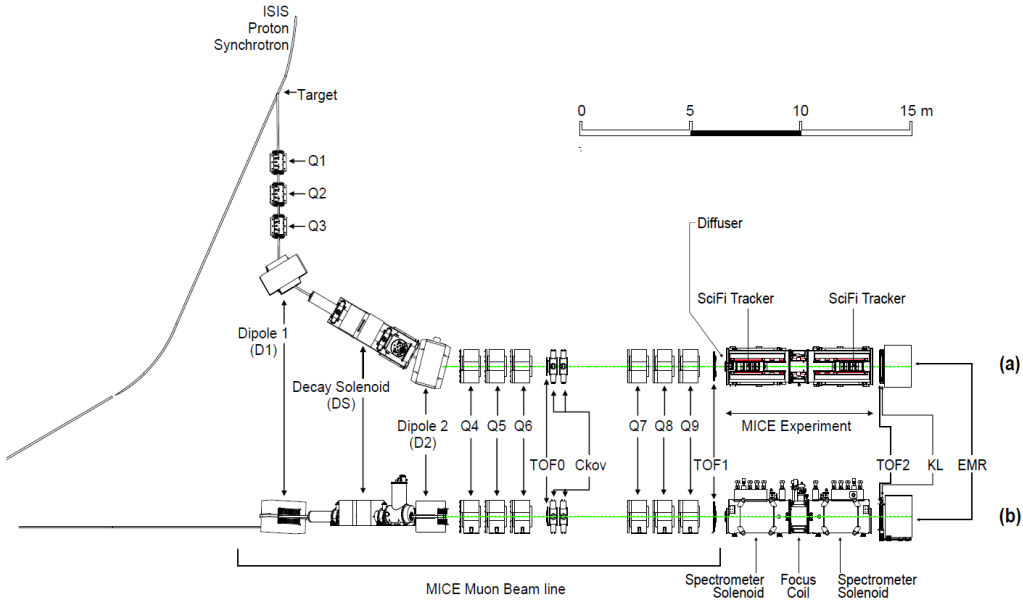


Figure 1: MICE experiment, showing the full beam line starting from the target position on the proton synchrotron) with the full set of quadrupoles and dipoles (Q1 to Q9, D1/2), the Decay Solenoid, and cooling channel elements with all the detectors.

Each TOF station was made of two planes of 1" scintillator bars oriented along X and Y directions, respectively. The bars were made of BC404 plastic scintillator. A simple fishtail light-guide was used to attach each end of each bar to R4998 Hamamatsu fast photomultiplier tubes. R4998 PMTs were delivered by Hamamatsu in assemblies (H6533MOD) that included the PMT tube, the voltage divider chain and a 1 mm thick  $\mu$ -metal shield, extending 30 mm beyond the photocathode surface. To increase the count-rate stability, active dividers were used. Illustration of a TOF detector is shown in figure 2 together with an exploded view of a slab.

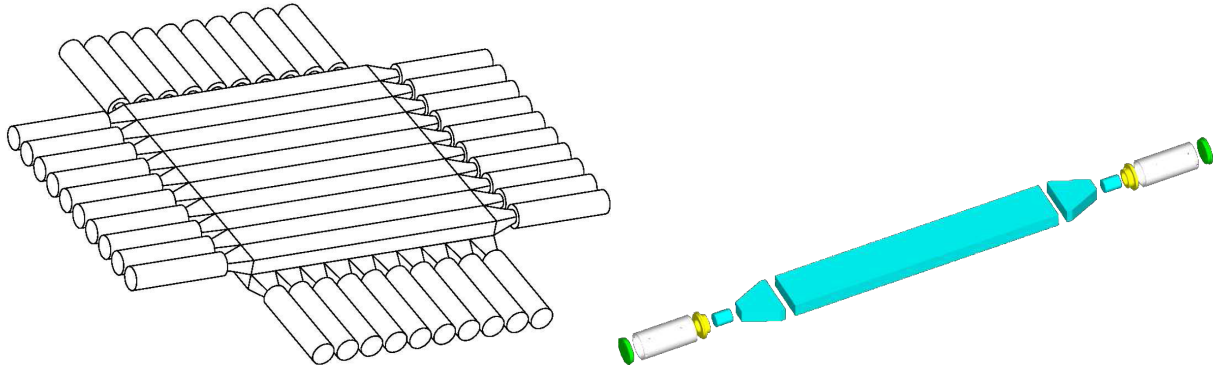


Figure 2: Design of the TOF detector structure showing the horizontal and vertical layers of slabs (left) and details of each slab showing one scintillator with on each side the light-guides and the PMTs (right) [4].

The stations TOF0, TOF1, and TOF2 had active areas of  $40 \times 40 \text{ cm}^2$ ,  $42 \times 42 \text{ cm}^2$ , and  $60 \times 60 \text{ cm}^2$  respectively. Each of the planes in TOF0 had 10, 4 cm wide, scintillator slabs. Stations TOF1 and TOF2 were composed by 7 and 10 scintillator slabs in each plane, respectively. The PMTs were connected to a 50% – 50% passive splitter using RG213 signal cable. One half of the signal was fed to the leading-edge CAMAC Lecroy 4115 discriminator followed by CAEN V1290 TDC for time measurement. The second half of the signal went to CAEN V1724 FADC for pulse-height measurement. Pulse height measurement was essential for time-walk

corrections. Each electronic issued a local readout trigger if signals in both PMTs attached to a slab crossed a specific threshold. All three stations were read out when TOF1 station issued a local trigger. This readout trigger was also used for the rest of the MICE detector systems.

All stations were exposed to residual magnetic fields: TOF0 was placed in a relatively low residual field produced by the last quadrupole magnet of the beam line (which had mirror plates installed), while the other two TOF stations were exposed to the stray fields of the cooling channel solenoids. A shielding structure was adopted covering all PMTs at each side of the stations [6].

The purpose of the TOF system was to discriminate particle species based on time-of-flight measurement. The main components in the MICE beam were muons, pions, and positrons. The time resolution needed to be sufficiently good to effectively discriminate between these types. At  $240 \text{ MeV}/c$ , the time-of-flight difference between muon and pion was about 1.3 ns between TOF0 and TOF1 stations. With 200 ps resolution, one reached near 100% discrimination efficiency [12].

### 2.1.1 Calibration Method

Measurement of time traversal of a particle through a TOF station was influenced by several factors at the hardware level. When a particle crossed the plastic scintillator, there was a short delay in light production, with a characteristic decay time of 1.8 ns.

After generation, scintillation light propagates to the ends of each scintillator slab where it was detected by photomultiplier tubes. The light-travel time depends on the distance of the particle crossing from the PMT. The lengths of slabs in TOF0, TOF1, and TOF2 were 40 cm, 40 cm, and 60 cm, respectively. This translates to about 3.0 ns, 3.1 ns, and 4.4 ns of light travel time, respectively, as the effective light propagation speed in the scintillator was found to be approximately 13.5 cm/ns. More delay was introduced by the transit time of each PMT and of the cable that led the signal to the readout electronics. These times were unique for each individual PMT channel and needed to be determined in dedicated measurements.

A simple linear discriminator measured the time of each signal coming from a PMT. This introduced bias in the measured time dependent on the total charge of the signal, an effect referred to as time-walk.

Signal times of each channel were recorded in TDC boards. Readout of the whole system was triggered by having a signal in TOF1. The readout trigger signal was distributed to all TDC boards and was used as a reference time. Which PMT channel's threshold crossing caused the readout was dependent on where the particle crossed through the TOF1 station. As a consequence, the reference time had a bias dependent on the position of the TOF1 crossing, an effect referred to here as trigger delay. To compensate this, the final time measurement in each station was determined as an average of the times of individual channels.

Corrections which needed to be made to the measured times were then the time-walk correction, the PMT channel specific delay time and a correction for the reference trigger time delay [13].

### 2.1.2 Reconstruction

A particle crossing a TOF station must have crossed 2 orthogonal slabs in the station's 2 planes. The time and approximate position of a particle crossing a TOF station was reconstructed from the PMT signals in the two slabs. Each slab with at least one recorded signal in each of the 2 PMTs was considered as being crossed by a particle. Times of these recorded signals were corrected for time-walk, readout trigger signal delay, and the channel specific delay. Time of crossing of the slab was then taken as the average of the 2 corrected PMT times.

The 2 slabs hit by a particle defined a pixel of area given by the width of the slabs. Sometimes, there were more slabs in each plane with signals. Matching of 2 slabs being crossed by a particle was done based on their

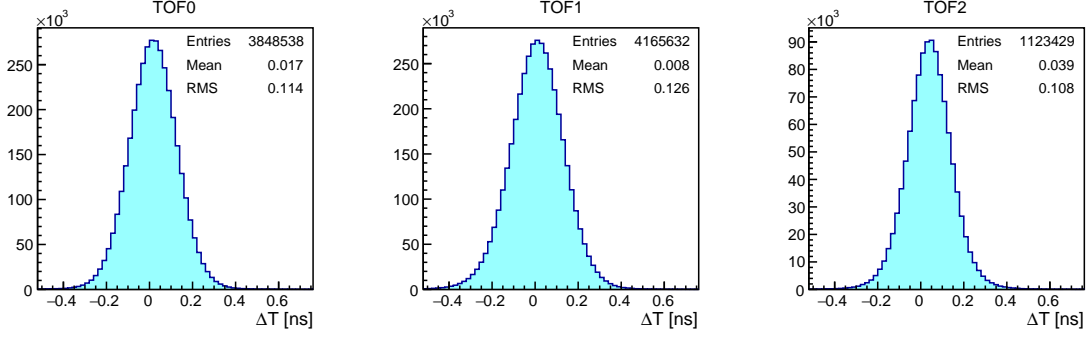


Figure 3: Overall slab  $\Delta T$  distributions. Total width of the distribution was due to the resolution of individual pixels and due to the offsets in their  $\Delta T$  distributions.

measured signal time. They were matched if the times were within a 4 ns window. The time of the particle crossing was determined as the average of times of the 2 matched slabs.

## 2.2 Performance

Resolution of time-of-flight measurement was given by time resolution of each station. The time associated to each TOF was determined from the average of the times when the two slabs (horizontal and vertical) were crossed by a particle. The resolution of the average was a half of the spread of their difference. Therefore, looking at slab  $\Delta T$  allowed the time-of-flight resolution to be determined.

Overall performance can be inferred from the combined slab  $\Delta T$  distributions. The plots in figure 3 show that they all centre approximately at 0 ns and they exhibit very similar resolutions, with TOF1 having the largest spread. Figure 4 shows an example of measurement of time of flight between the first two stations, TOF0 and TOF1. Times of electrons, muons, and pions are clearly separated, creating peaks from left to right, respectively. The observed width of the electron peak of approximately 0.11 ns was about 30% larger than the calculated spread from a naive addition of slab  $\Delta T$  of the individual TOF stations. This difference was attributed to contributions to the resolution of individual stations which cancel out in the slab  $\Delta T$  measurement, and to variations in the travelled path length of the electrons between stations TOF0 and TOF1.

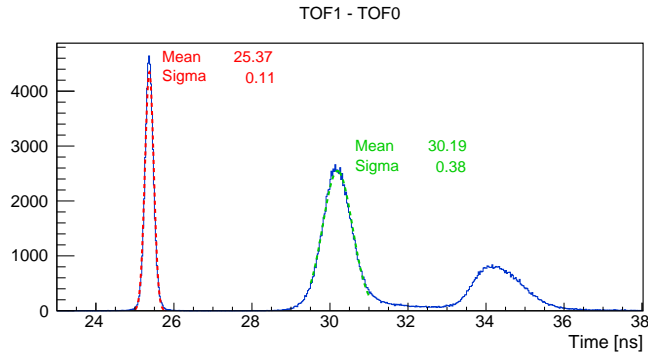


Figure 4: Time of flight between TOF0 and TOF1 for a “pion” beam after all corrections have been applied. From the left: the well separated electron, muon and pion peaks.

<sup>110</sup> **3 Cherenkov Detectors**

### 3.1 Introduction

The MICE threshold Cherenkov detectors, measuring velocity, were primarily designed to provide  $\pi$ - $\mu$  separation in the higher momentum ranges, where TOF separation of the two species peaks was not sufficient for conclusive particle identification.

<sup>115</sup> In order to provide separation over a large range of momenta, two high-density silica aerogel Cherenkov detectors (CkovA and CkovB) with refractive indices  $n=1.07$  and  $n=1.12$  were used. Light was collected in each counter by four eight-inch UV-enhanced PMTs and recorded by CAEN V1731 FADCs (500 MS/s). The two detectors were placed directly one after another in the beamline, located just after the first TOF counter. In figure 5 an exploded view of one detector was shown.

<sup>120</sup> Their respective thresholds provided different responses in four distinct momentum ranges, i.e. in the  $200\text{ MeV}/c$  beams, pions were below the threshold which would fire the detector for both CkovA and CkovB whereas muons were above the threshold only for CkovB, while for the  $240\text{ MeV}/c$  beams, pions were above the threshold for CkovB while muons were above for both CkovA and CkovB. This can be used to distinguish particle species. Below the CkovB muon threshold of about  $217.9\text{ MeV}/c$ , where there was no separation, the TOFs provided good separation, whereas the momentum range above the CkovA pion threshold <sup>125</sup>  $367.9\text{ MeV}/c$  was outside of the MICE running parameters [14]. For unambiguous identification of particle species the Cherenkov detectors would need a momentum measurement from the MICE tracker.

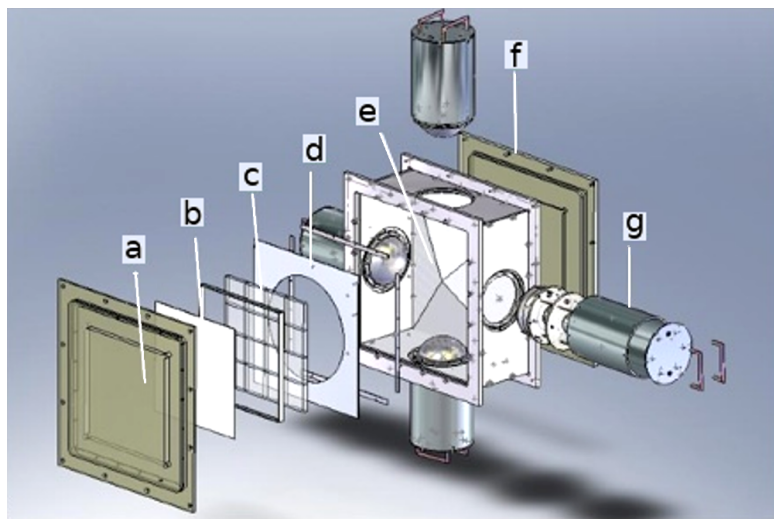


Figure 5: MICE aerogel Cherenkov counter blowup: a) entrance window, b) mirror, c) aerogel mosaic, d) acetate window, e) GORE reflector panel, f) exit window and g) eight-inch PMT in iron shield.

### 3.2 Performance

A wide range beam momenta (including alignment runs) has been used in order to cover the full spectra of <sup>130</sup> particles that could have been measured by the Cherenkov detectors. The asymptotic light yield (for  $\beta=v/c=1$ ) in each counter were measured using the electron peaks, giving  $16 \pm 1$  photoelectrons (NPE) in CkovA and  $19 \pm 1$  in CkovB.

The photoelectrons yields versus momentum for muons and pions in CkovA and CkovB are displayed in figure 6, using the time of flight between TOF0 and TOF1 to select the species and to estimate the momentum.  
135 The distributions  $N(P)$  of NPEs as a function of the momentum  $P$  were fitted with the function

$$N(P) = N_0 + N_{\beta=1} \left( 1 - \left( \frac{P_0}{P} \right)^2 \right) \quad (1)$$

where  $N_0$  is the number of background photoelectrons,  $N_{\beta=1}$  is the asymptotic light yield and  $P_0$  is the momentum threshold.

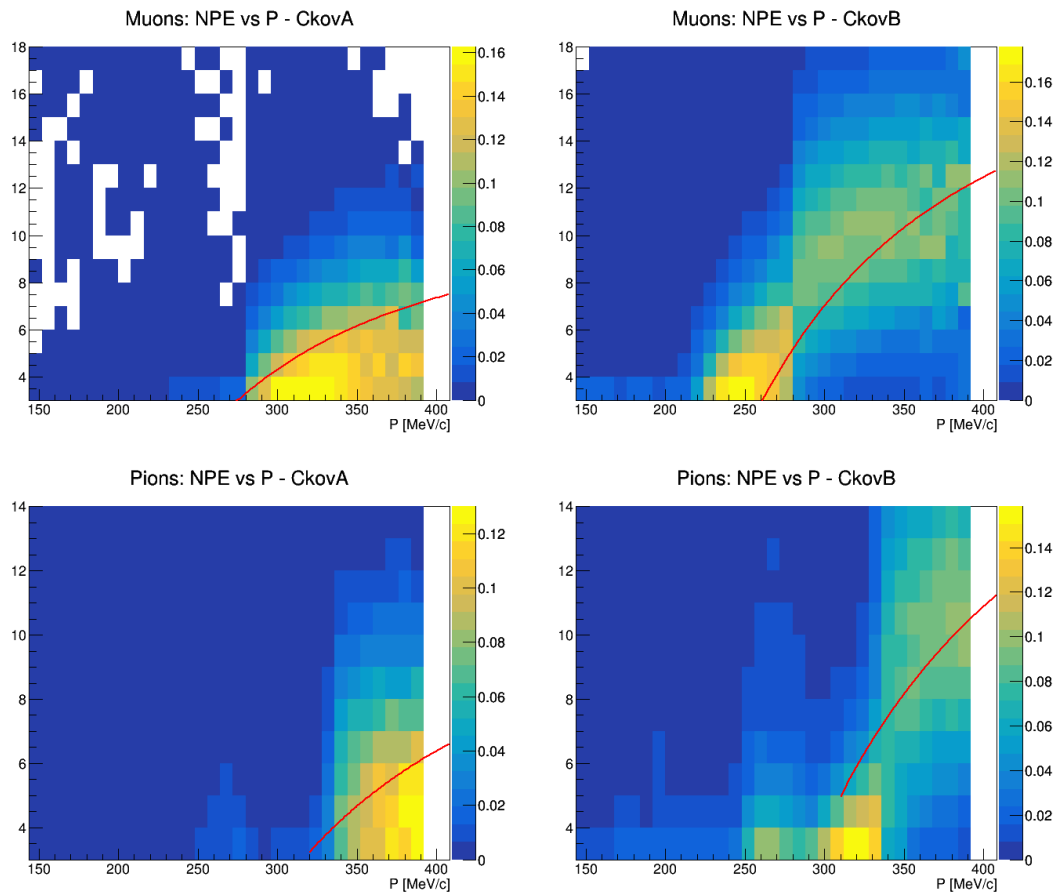


Figure 6: Photoelectron yields versus momentum for muons and pions in CkovA and CkovB with the superimposed fitted activation functions.

The observed muon thresholds were  $267.3 \pm 18.1$  and  $219.4 \pm 14.5$  MeV/c, while for pions were  $332.2 \pm 38.4$  MeV/c and  $295.9 \pm 95.9$  MeV/c, respectively in CkovA and CkovB. The  $NPE_{\beta=1}$  values were generally  
140 lower than the values predicted as in a previous analysis [14]: this was mostly due to TOF0 acting as a pre-shower radiator.

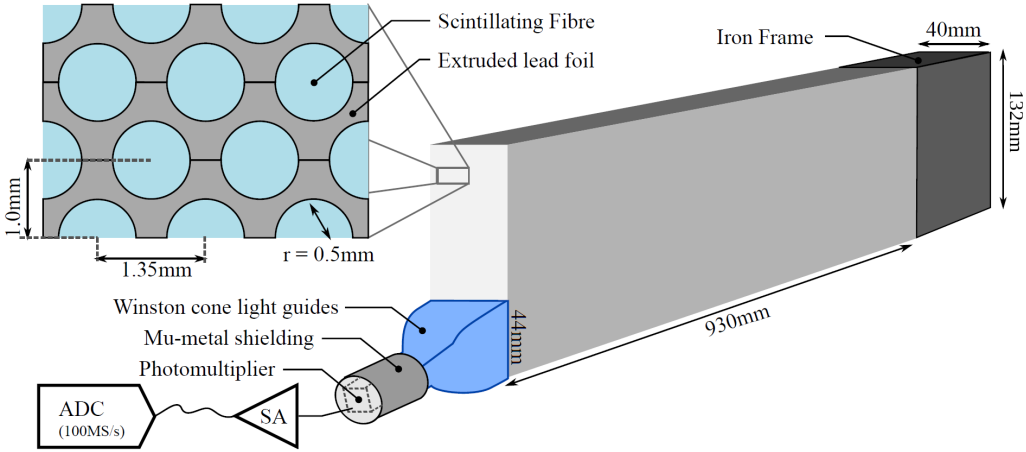


Figure 7: Single slab design of MICE KLOE-Light Calorimeter.

## 4 KLOE-Light Calorimeter

### 4.1 Introduction

The KLOE-Light (KL) pre-shower sampling calorimeter was composed of extruded lead foils in which scintillating fibres were placed in. The volume ratio of scintillator and lead was approximately 2 to 1, “lighter” than the one of the KLOE experiment calorimeter (1 to 1).

The fibres were 1 mm diameter BICRON BCF-12, scintillating in the blue, 1.35 mm distant from each other within a layer. The distance between two layers was 0.98 mm, one layer being shifted by half the fibre pitch with respect to the next. Scintillation light was guided from each slab into a total of six PMTs (three on each side). Iron shields were fitted to each photomultiplier to mitigate against large stray magnetic fields from the cooling channel. The signal from each PMT was sent to a shaping amplifier (SA) module, which shapes and stretches the signal in time in order to match the sampling rate of the flash ADCs (figure 7 shows the design of a single slab). A total of 7 slabs forms the whole detector, which has an active volume of  $93\text{ cm} \times 93\text{ cm} \times 4\text{ cm}$ .

With its 2.5 radiation lengths the KL was used to distinguish muons from decay electrons providing energy deposition and timing information and to act as pre-shower in front of the EMR. The detector has been used to estimate the level of pion contamination within the MICE muon beams to be around 1% [11].

### 4.2 Performance

The study of the KL response to different particle types (muons, pions and electrons) at different momenta was based on particle identification obtained by time-of-flight detector, as shown in the example of figure 4, by applying time cuts on the time-of-flight spectrum across the peaks of the different species. The performance is presented for beamline settings with nominal 140, 170, 200, 240 and 300 MeV/c momenta. The results presented below are obtained from the straight tracks runs (i.e. without magnetic fields in the trackers or focus coil). The KL response to muons, pions and electrons for all available momenta is presented in figure 8. It is clear in the cases of muons and pions that they were below the minimum ionizing particle momenta since energy deposition decreases with momentum increasing. Actually the energy deposition is defined as the sum of ADC products from all cells in KL above a given threshold. The ADC product on the other hand is the product of left and right side of one slab divided by the sum of left and right side:  $\text{ADC}_{\text{prod}} = 2 \times \text{ADC}_{\text{left}} \times \text{ADC}_{\text{right}}$

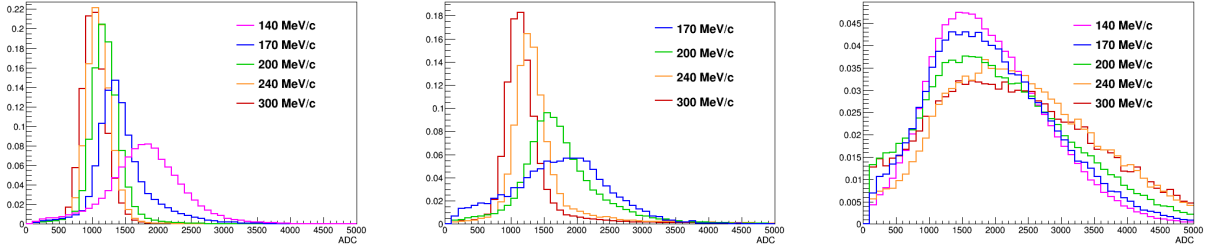


Figure 8: KL response to muons (left), pions (centre) and electrons (right) for all available momenta. The charge deposited by particles in KL in arbitrary units is shown. All histograms are normalised to unity.

$\text{ADC}_{\text{right}} / (\text{ADC}_{\text{left}} + \text{ADC}_{\text{right}})$ . The factor 2 is present for normalisation. The product of two sides compensates the effect of attenuation.

For comparison of energy deposition of muon, pions and electrons for a fixed momentum is presented in figure 9. For example 300 MeV/c (figure 9, bottom) muons and pions have almost the same distribution, while moving to lower energies pions have a broader distribution, experiencing hadronic interactions and loosing more energy. This pion behaviour has been used to estimate its contamination in muon samples [11].

Species	140 MeV/c	170 MeV/c	200 MeV/c	240 MeV/c	300 MeV/c
<b>electrons</b>	$0.95 \pm 0.02$	$0.95 \pm 0.01$	$0.94 \pm 0.03$	$0.96 \pm 0.02$	$0.95 \pm 0.02$
<b>muons</b>	$0.97 \pm 0.02$	$0.99 \pm 0.01$	$0.99 \pm 0.01$	$0.99 \pm 0.01$	$0.99 \pm 0.01$
<b>pions</b>	n/a	$0.89 \pm 0.03$	$0.95 \pm 0.03$	$0.97 \pm 0.03$	$0.98 \pm 0.01$

Table 1: Efficiency of KL for electrons, muons and pions as a function of particle momentum. The conditions required are existing of a TOF track and signal in KL above the threshold. The uncertainties are statistical.

In figure 10 is shown simulation of KL response to 300 MeV/c muons and pions and the distributions are compared with data. The simulation takes into account the distribution of the photon in scintillator fibres, the subsequent creation of photoelectrons on photomultiplier photocathodes and the response of the photomultipliers (which gain was around  $2 \times 10^6$ ). The agreement between data and simulation was very good.

## 5 Electron Muon Ranger

### 5.1 Introduction

The Electron-Muon Ranger (EMR) was a fully-active scintillator detector [15]. It could be classified as a tracking-calorimeter as its granularity allowed for track reconstruction. The EMR consisted of extruded triangular scintillator bars arranged in planes. One plane contained 59 bars and covered an area of  $1.27 \text{ m}^2$ . Each even bar was rotated by  $180^\circ$  with respect to the odd one. A cross-section of bars and their arrangement in a plane is shown in figure 11. This configuration did not leave dead areas in the detector for particles crossing a plane with angles that would not exceed  $45^\circ$  with respect to the beam axis. Each plane was rotated through  $90^\circ$  with respect to the previous one, such that hits in a pair of neighbour planes defined a horizontal and vertical ( $x, y$ ) interaction coordinate. The light, produced when a particle crossed a bar, was collected by a wave-length shifting (WLS) fibre glued inside the bar. At both ends, the WLS fibre was coupled to clear fibres that transport the light to a PMT. Signals produced in a plane were read out collectively on one end by a single-anode PMT

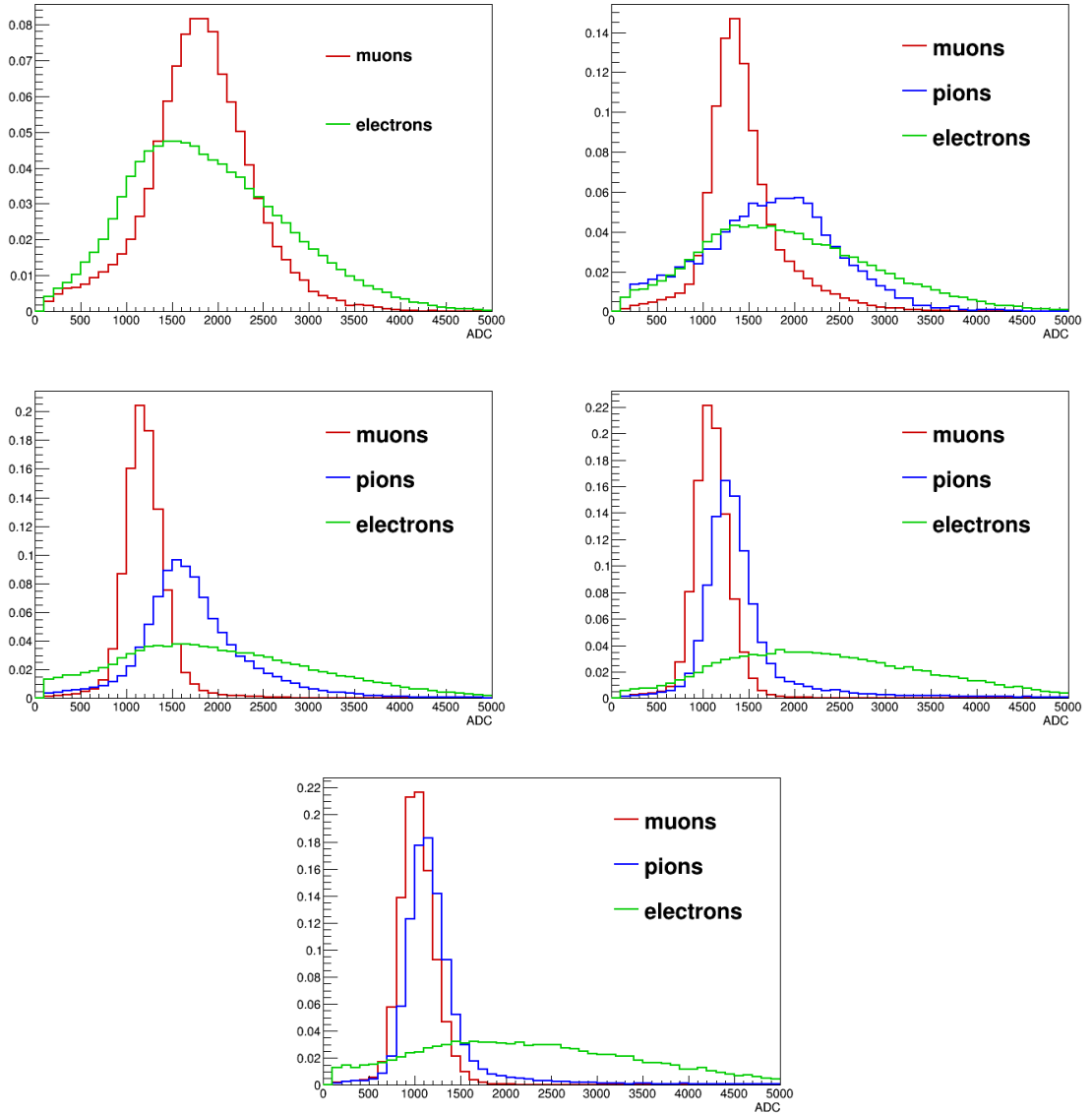


Figure 9: Comparison of energy deposition of muons, pions and electrons at 140 MeV/ $c$  (top left), 170 MeV/ $c$  (top right), 200 MeV/ $c$  (middle left), 240 MeV/ $c$  (middle right) and 300 MeV/ $c$  (bottom).

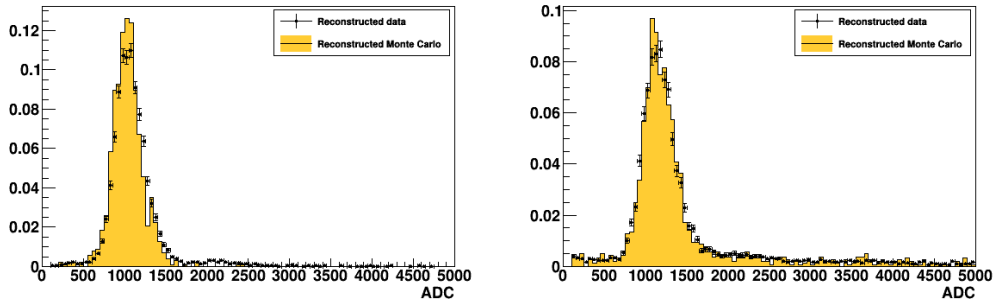


Figure 10: Comparison between data and Monte Carlo simulation of KL response to muons (left) and pions (right) at 300 MeV/ $c$ .

190 (SAPMT) for an integrated charge measurement and separately on the other by multi-anode PMTs (MAPMT) for individual bar hit reconstruction. The full detector was composed of 24 X-Y modules for a total active volume of approximately 1 m<sup>3</sup>.

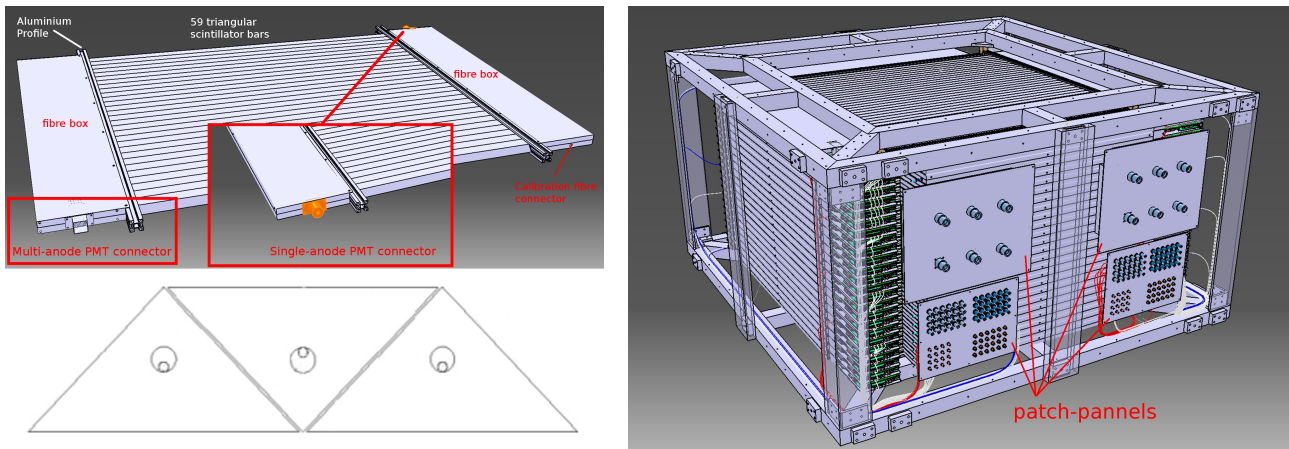


Figure 11: Drawing of one EMR plane (top left), cross section of 3 bars and their wavelength shifting fibres (bottom left) and drawing of the full detector and its supporting structure (right).

195 An array of analyses were conducted to characterise the hardware of the EMR and determine whether the detector performed to specifications [16]. The clear fibres coming from the bars were shown to transmit the desired amount of light, and only four dead channels were identified. The level of crosstalk was within acceptable values for the type of multi-anode photomultiplier used with an average of  $0.20 \pm 0.03\%$  probability of occurrence in adjacent channels and a mean amplitude equivalent to  $4.5 \pm 0.1\%$  of the primary signal intensity. The efficiency of the signal acquisition, defined as the probability of recording a signal in a plane when a particle goes through it in beam conditions, was  $99.73 \pm 0.02\%$  [15].

200 The primary purpose of the EMR was to distinguish between muons and their decay products, identifying muons that have crossed the entire cooling channel. Muons and electrons exhibited distinct behaviours in the detector. A muon followed a single straight track before either stopping or exiting the scintillating volume. Electrons showered in the lead of the KL and created a broad cascade of secondary particles. Two main geometric variables, the plane density and the shower spread, were used to differentiate them. The detector 205 was capable of identifying electrons with an efficiency of 98.6 %, providing a purity for the MICE beam that exceeds 99.8 %. The EMR also proved to be a powerful tool for the reconstruction of muon momenta in the range 100–280 MeV/c [17].

## 5.2 Performance

210 The performance of the EMR detector was assessed at three levels of resolution with data acquired during different period of data taking. The performance of the hardware itself was evaluated by analysing the characteristics of raw photomultiplier signals. The reconstruction efficiency was assessed. The performance of the detector as an electron tagging device was measured.

### 5.2.1 Hardware efficiencies

The MICE beam line was tuned to the highest attainable momentum to maximise the transmission to the EMR detector and increase the range of particles in the detector (approximately 400 MeV/c). In this configuration the beam line produces pions and muons in comparable quantities, along with positrons. The particle species were identified by evaluating their time-of-flight between TOF1 and TOF2. Only the particles with a time-of-flight between 28 and 28.75 ns, i.e. compatible with the muon hypothesis, were included in the analysis sample.

A muon that makes it into the analysis sample has a momentum larger than 350 MeV/c right before TOF2.

It was expected to cross both TOF2 and the KL without stopping and penetrate the EMR. In practice, the probability of creating an EMR event, i.e. to produce hits in the detector was  $99.62 \pm 0.03\%$ . The minor inefficiency may be attributed to pions in the muon sample that experienced hadronic interactions in the KL. If hits were produced in the detector, space points were reconstructed  $98.56 \pm 0.06\%$  of the times. The inefficiency may be associated with muons that decay between TOF2 and the EMR and produced scarce hits in the detector.

To evaluate the efficiency of the scintillator planes and their readouts, only the muons which penetrated the entire detector were used. If a signal was recorded in the most downstream plane, it was expected that at least a bar will be hit in each plane on its path and that a signal will be recorded in the single anode PMT. In  $3.26 \pm 0.02\%$  of cases, on average, a plane traversed by a muon will be not produce a signal in its MAPMT and that the most probable amount of bars hit was one, while a track was missed by an SAPMT  $1.88 \pm 0.01\%$  of the time.

### 5.2.2 Electron rejection

The main purpose of the EMR was to tag and reject the muons that have decayed in flight inside the experimental apparatus. A broad range of beam line momentum settings was used to characterise the muon selection efficiency. The particle species were characterised upstream of the detector by using the time-of-flight between TOF1 and TOF2 as shown before. The limits of the peaks were fitted to each setting in order to separate the muons and positrons into two templates upstream of the EMR. Particles that fell above the upper limit of the muon peak were either pions or slow muons and were rejected from this analysis.

MICE was a single-particle experiment, i.e. the signals associated with a trigger originated from a single particle traversing the detector. The multi-anode readout of each detector plane provided an estimate of the position of the particle track in the  $xz$  or the  $yz$  projection, depending on the orientation of the scintillator bars. Inside the detector the muon exhibited a clean straight track while the positron showers inside the lead of the KL and produces a disjointed and spread-out signature. Two particle identification variables based on these distinct characteristics can be defined. One is the plane density,  $\rho_p$ , defined as

$$\rho_p = \frac{N_p}{Z_p + 1}, \quad (2)$$

where  $N_p$  is the number of planes hit and  $Z_p$  the number of the most downstream plane. A muon deposits energy in every plane it crosses until it stops, producing a plane density close to one. A positron shower contains photons that may produce hits deep inside the fiducial volume without leaving a trace on their path, reducing the plane density. The second variable is the normalised chi squared,  $\hat{\chi}^2$ , of the fitted straight track, i.e.

$$\hat{\chi}^2 = \frac{1}{N - 4} \sum_{i=1}^N \frac{\text{res}_{x,i}^2 + \text{res}_{y,i}^2}{\sigma_x^2 + \sigma_y^2}, \quad (3)$$

where  $N$  is the number of space points (one per bar hit),  $\text{res}_{q,i}$  the residual of the space point with respect to the track in the  $qz$  projection and  $\sigma_q$  the uncertainty on the space point in the  $qz$  projection,  $q = x, y$  [18]. The

number of degrees of freedom is  $N - 4$ , as a three-dimensional straight track has four parameters. This quantity represents the transverse spread of the particle's signature. A muon follows a single track and is expected to have a  $\chi^2$  close to one, while an electron shower is expected to produce a larger value. The two discriminating variables can be combined to form a statistical test on the particle hypothesis. Dense and narrow events will be tagged as muons while non-continuous and wide electron showers will not. The quality of a test statistic may be characterised in terms of the loss,  $\alpha$ , the fraction the muon sample that is rejected, and the contamination,  $\beta$ , the fraction of the electron sample that is selected.

The downstream tracker allows for the reconstruction of particle momentum before entering the EMR. To assess the influence of momentum on contamination and loss, their values were calculated, because of the resolution, for 10 MeV/c bins in the range 100–300 MeV/c. The test statistic calculated in each bin was based on the optimal set of cuts optimised for the whole sample, i.e.  $\rho^* = 86.131\%$  and  $\chi^{2*} = 14.229$ . Figure 12 shows the loss,  $\alpha$ , and the contamination,  $\beta$ , as a function of the momentum measured in TKD. It shows that, at low momentum, the apparent muon loss increases. This is due to an increase in decay probability between TOF2 and the EMR and an decrease in the number of muons that cross the KL to reach the EMR.

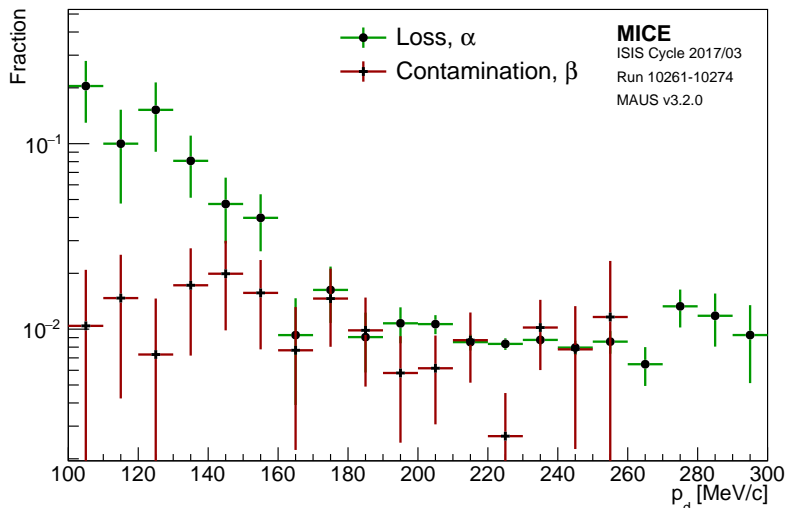


Figure 12: Percentage of electron contamination,  $\beta$ , and muon loss,  $\alpha$ , for different ranges of momentum measured in the downstream tracker,  $p_d$ . The error bars are based on the statistical uncertainty in a bin.

## 6 Trackers

### 255 6.1 Introduction

MICE was equipped with two identical, high precision scintillating-fibre trackers, described in [19]. One tracker, TKU, was upstream of the cooling cell, the other, TKD, was downstream, the mirror image of TKU as shown in figure 1. Each tracker was placed in a superconducting solenoid (SSU and SSD, upstream and downstream respectively) designed to provide a uniform magnetic field over the tracking volume.

260 The trackers were 110 cm in length and 30 cm in diameter (see figure 13). There were five stations per tracker (labelled 1 to 5, with station 1 being closest to the cooling cell) held in position using a carbon-fibre space-frame. The stations sit at different distances in  $z$  (beam axis) of 20–35 cm: this ensured that the azimuthal rotation of track position from one station to the next differs, difference being important in the resolving ambiguities at

the pattern-recognition stage. Each tracker was instrumented with an internal LED calibration system and four  
265 3-axis Hall probes to monitor the field.



Figure 13: Photograph of one of the MICE Trackers, showing the five stations and the three doublet planes of scintillating fibres, each plane at  $120^\circ$  angles to the next (the central fibres of plane can be seen as darker lines traversing the station). Bundles of seven  $350\ \mu\text{m}$  fibres were grouped together, to be read out by 1 mm scintillating fibre light guides.

The tracker stations consisted of three doublet layers of  $350\ \mu\text{m}$  scintillating fibres, these layers were arranged such that each was at an angle of  $120^\circ$  with respect to the next. This arrangement ensured that there were no inactive regions between adjacent fibres. Bundles of seven fibres were grouped into a single readout channel (this reduced the number of readout channels, while maintaining position resolution). The trackers had a spatial  
270 resolution per doublet layer of  $470\ \mu\text{m}$  and an expected light yield of approximately 10 photo-electrons.

The light from the seven scintillating fibres passed into a single clear fibre, which took it to a visible light photon counter (VLPC) which operated at 9 k. The signals from the VLPCs were digitised using electronics developed by the D0 collaboration [20].

## 6.2 Performance and Reconstruction

275 Each of the 15 tracker planes (three per station and five stations) consisted of 214 channels, labelled 0–213, likewise each plane was assigned an integer plane number 0–2. Particle signals were recorded by the tracker electronics and calibrated channel by channel then converted into signal NPE. This information was then used to form a digit and was the first step in tracker reconstruction. Digit profiles were useful in identifying and rectifying or removing hot or dead channels in the planes and ensuring the accuracy of calibration. Smooth  
280 centrally peaked spectra were expected in a plane with no dead channels and minimal electronics noise, but this was not an essential requirement since it was the combination of two or three planes which go to make a point in the track and so there was redundancy built in. Hence a significant proportion of individual channels can be lost without a knock on drop in efficiency. The clustering algorithm looped over every combination of pairs of digits in a single event and combined any that occur in neighbouring channels. In the case of a  
285 multi-digit cluster, the unweighted average channel value was used to define the plane coordinate and the NPE was summed.

For each station the constituent planes were searched for clusters that can be used to form a spacepoint. Spacepoints were constructed from clusters from all three planes (a triplet spacepoint) or from any two out of

the three planes (a doublet spacepoint).

### 290 6.2.1 Noise

The scintillating fibre trackers operated by registering digits above a given NPE threshold within each fibre plane. Fibres were collected into channels as ganged bundles of 7 for each channel, with digits were registered per channel instead of per fibre. From a coincidence of digit events in 2 or 3 oblique fibres (fibres in differing planes), a spacepoint was reconstructed, from which track reconstruction can occur. We considered noise in the tracker to be those digits registered not from the passage of a beam particle, but instead from other sources, for instance, dark current from thermal electron emission in the PMTs. To isolate noise from signal during beam-on data collection, a strict cut can be made requiring that only events with one fitted track and 5 spacepoints per tracker were selected, with all 5 spacepoints included in the fitted track. All digits corresponding to the track were then removed from the total set of digits for that event, and the remainder were considered noise digits. An in-situ approximation of active channels for the current data-taking period was made, assuming all channels without at least one registered digit in the selected data-taking run were inactive. The average noise rate per channel per event was then calculated as the total number of event digits above the considered NPE threshold in each tracker, divided by both the active channel number and the number of events satisfying the above selection criteria. This gave a value of 0.18% upstream and 0.06% downstream for events above 2 NPE.

### 305 6.2.2 Track Finding Efficiency

Data were analysed in order to determine the track and spacepoint finding efficiency of the detectors during running conditions. A time-of-flight cut was used to ensure that each measured track had a time-of-flight consistent with a muon throughout the entire experimental apparatus. A hit was therefore required in each of the TOF1 and TOF2 detectors, which ensured that the particle must have been successfully transmitted through the cooling channel, crossing both tracking detectors. These requirements ensured that there was a better than 99.9% probability that a particle will have traversed a tracking detector. The number of events missing a track was therefore measured and used to estimate the efficiency of the detector. The results of the efficiency analysis were tabulated in table 2 for a range of momentum and nominal emittances. A track-finding efficiency of 98.70% was reported for the upstream tracker and 98.93% for the downstream tracker, averaged over field and beam conditions. Additionally, assuming a track was found, the probability of successfully finding each spacepoint is summarised in table 3. The overall efficiency of both trackers was sufficient to not present any significant systematic uncertainties in the analysis, however it was lower than the ideal expectation, 99.9% efficiency, due to the presence of dead channels, an unavoidable feature of the construction process.

Momentum	Nominal Emittance	No. Events	Upstream Tracks Found	Downstream Tracks Found
200 MeV/c	6mm	221879	99.42%	96.07%
200 MeV/c	3mm	215229	98.38%	99.19%
140 MeV/c	6mm	180283	98.37%	99.16%
140 MeV/c	10mm	130859	98.47%	98.93%
Averaged		748250	98.70%	98.21%

Table 2: The track finding efficiency for the upstream and downstream trackers for 140 MeV/c and 200 MeV/c beams, and for 3, 6 and 10 mm nominal emittances.

Momentum	Nominal Emittance	No. Events	Upstream Spacepoints Found	Downstream Spacepoints Found
200 MeV/c	6mm	221879	99.41%	94.63%
200 MeV/c	3mm	215229	98.04%	97.41%
140 MeV/c	6mm	180283	97.99%	99.16%
140 MeV/c	10mm	130859	98.07%	97.44%
Averaged		748250	98.44%	97.01%

Table 3: The spacepoint finding efficiency, assuming the presence of a track, for the upstream and downstream trackers for 140 MeV/c and 200 MeV/c beams, and for 3, 6 and 10 mm nominal emittances.

### 6.2.3 Track Fit Predicted Performance

- 320 Monte Carlo simulation used with realistic field and beam conditions in order to estimate the reconstruction performance. A beam centred at 140 MeV/c with 10 mm nominal emittance, representing a typical data set, was used for the study of emittance evolution. Results were presented in figure 14 for the upstream tracker and figure 15 for the downstream tracker.

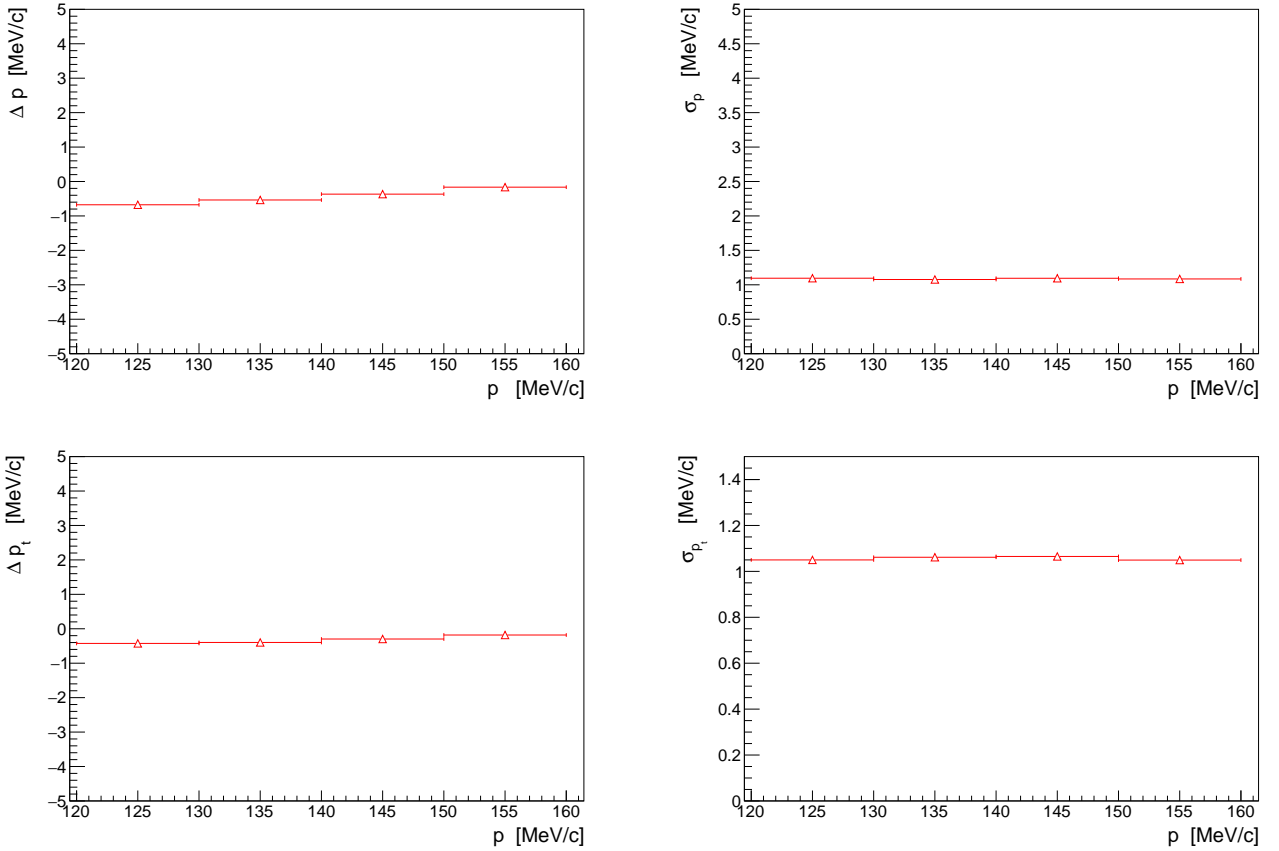


Figure 14: Predicted momentum reconstruction bias (left) and resolution (right) for the longitudinal (top) and transverse (bottom) momentum components in the upstream tracker.

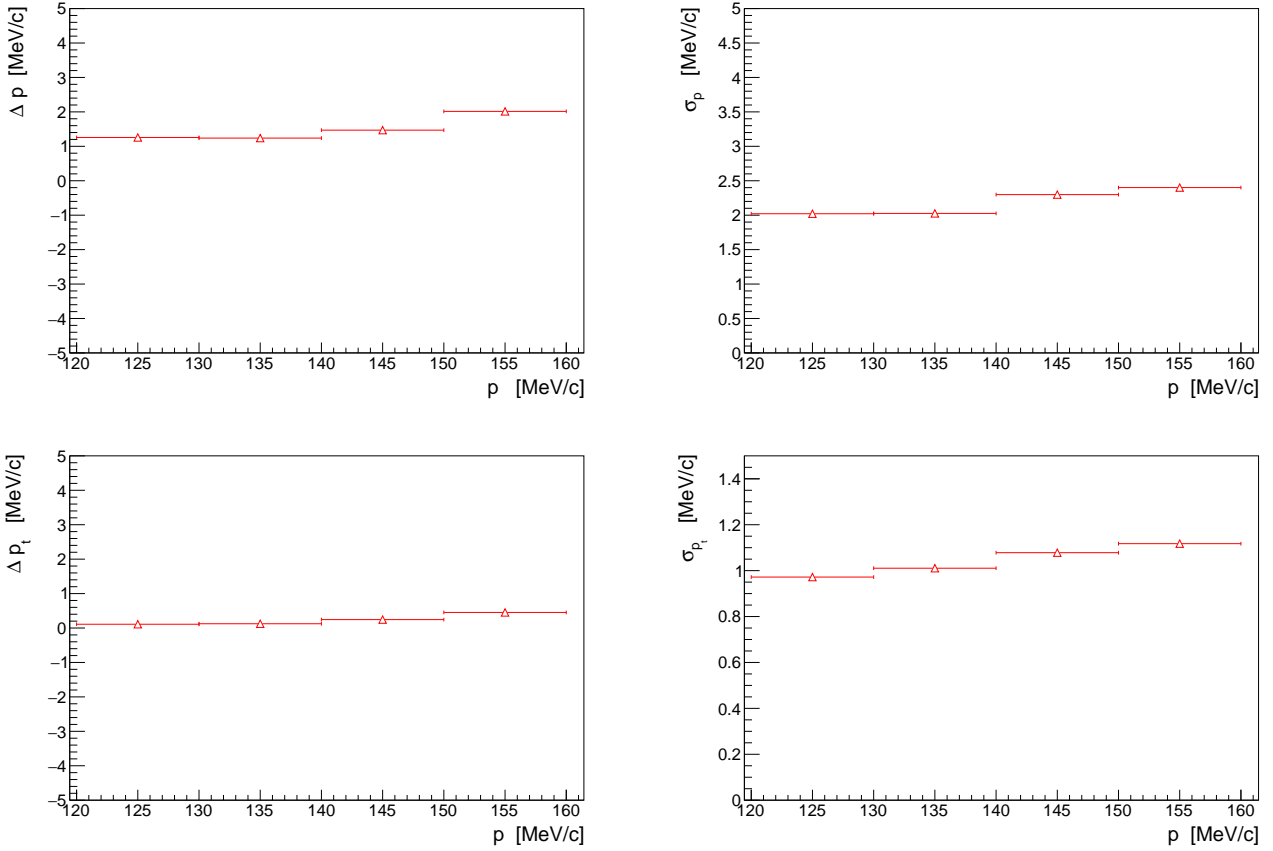


Figure 15: Predicted momentum reconstruction bias (left) and resolution (right) for the longitudinal (top) and transverse (bottom) momentum components in the downstream tracker.

### 6.3 Efficiency evolution

325 The efficiency of the tracker was processed over the lifetime of its use during the data taking. The analysis used in section 6.2.2 was repeated and automated for runs starting in 2015. The selection included two more constraints: was required a spacepoint to be reconstructed within the tracker volume using a radial cut and that only a single spacepoint was reconstructed in each of the stations, as generally required in most of the analysis. The evolution of the straight and helical track finding efficiency in the upstream and downstream trackers is  
330 shown in figure 16, showing efficiencies generally above 99.0%.

## 7 Global Track Matching Reconstruction

The overall detector performance could be validated by extrapolating tracks from one detector to another and comparing the reconstructed coordinates with the extrapolated values. Tracks measured in the upstream tracker were extrapolated upstream to TOF1 and TOF0, and downstream to TKD and TOF2. Where there are materials 335 in the beamline, the energy change on passing through the material was estimated using the most probable energy loss. Material thicknesses were approximated by the on-axis thickness.

Particles entering the analysis must satisfy the following criteria:

- at least one space point must be reconstructed in TOF2;
- one track must be reconstructed in both TKU and TKD. The track in TKD must extrapolate to within the active area of TOF2; and

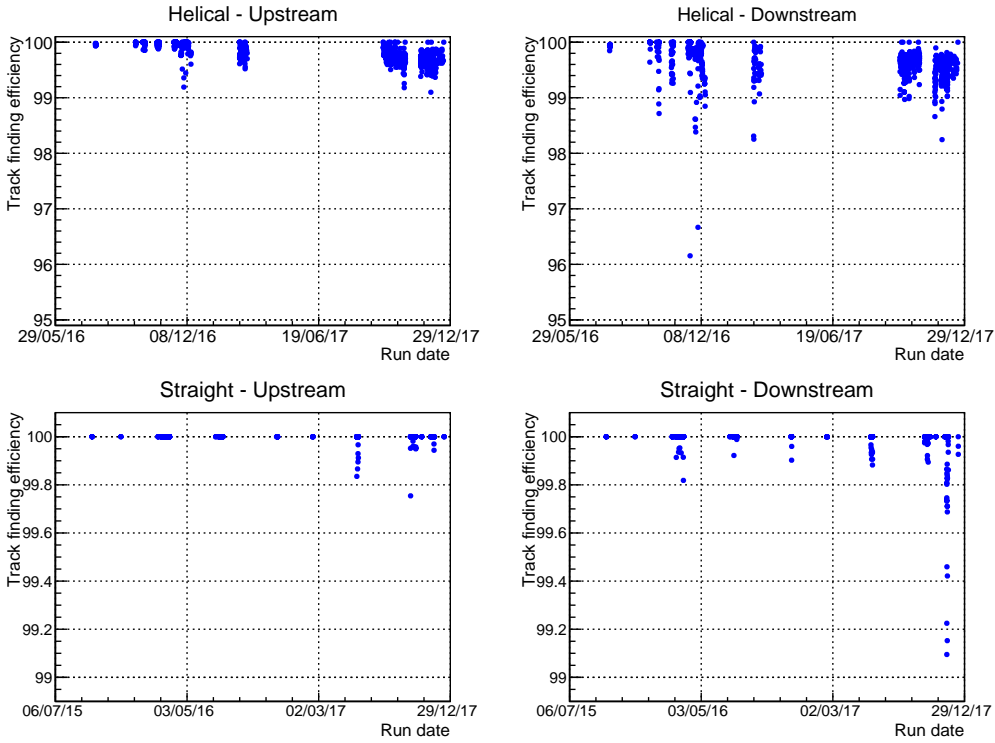


Figure 16: Evolution of the straight and helical track finding efficiency over time for the upstream (left) and downstream (right) trackers during the key periods of data taking since 2015.

- the track found in TKD must lie within a radius of 100 mm from the beam axis at the following apertures: the upstream absorber safety window; the upstream absorber window; the absorber centre; the downstream absorber window; the downstream absorber safety window; the upstream edge of SSD; the helium window in SSD; the downstream edge of the downstream PRY aperture.

345 The final cut restricted the sample to events in which particles were contained within the active area of the experiment and ensured that the selection was consistent across the configurations in which data was taken.

## 8 Beam-based Detector Alignment

### 8.1 Introduction

A beam-based alignment algorithm was developed to improve the resolution on the position of the scintillating-fibre trackers lodged inside the bores of superconducting magnets. This method was used to determine the azimuthal orientation of the trackers with a resolution of  $6 \text{ mrad}/\sqrt{N}$  and their position with a resolution of  $20 \text{ mm}/\sqrt{N}$ , where  $N$  the number of selected tracks [21].

The starting point for the beam-based alignment was the geometrical survey of the detectors in the MICE Hall which was performed using laser telemetry. Only the trackers, nested in the superconducting solenoids, could 355 not be accessed, so their position was inferred with respect to the flanges of the solenoids and the beam-based alignment was used to verify their alignment.

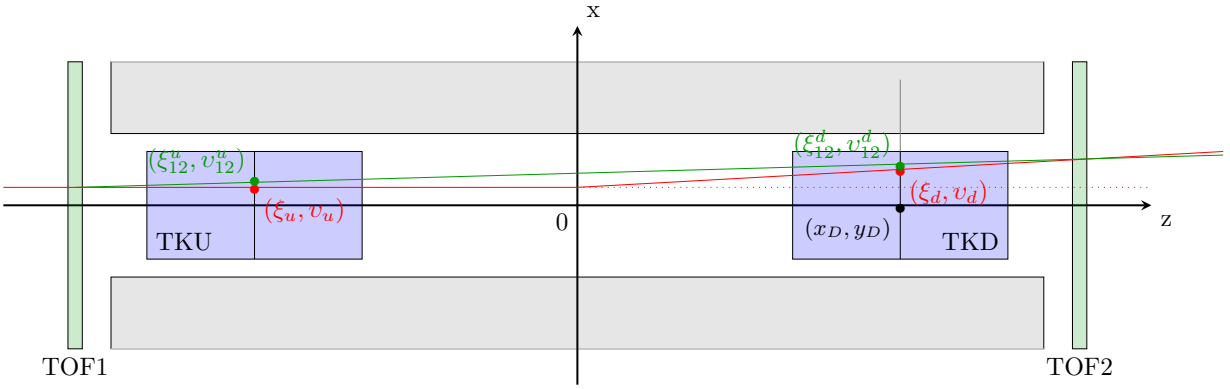


Figure 17: True path of a single particle track (red) and its path as reconstructed from the time-of-flight system (green). The position of the track at the tracker centres is represented by markers.

## 8.2 Analysis method

The position of each tracker in global coordinates was entirely defined by the location of its centre and a set of three angles. Since the position of each tracker along the beamline was known to great accuracy from the survey  
 360 and the rotation about  $z$  has a negligible influence on the alignment, only 4 constants had to be determined for each tracker.

The location of the TOFs was used as the reference for the tracker alignment. The line that joins the centre of TOF1 with the centre of TOF2 was chosen to be the reference axis. A deviation from this axis was considered as a misalignment of the trackers. Multiple scattering in the beam line would not allow formed alignment on  
 365 single-particle basis. For example, figure 17 shows the path of a single particle that scatters in the absorber module of the MICE experiment. The mean residual angles and positions of the trackers with respect to the TOF1–TOF2 axis were evaluated to allow the correction factors to be determined.

Each TOF provided a single space point in the global coordinate system. This position was assumed to be the true position with a large uncertainty due to the limited granularity of the detector. Trackers sampled the  
 370 particle track in five different stations and this allows for the reconstruction of a straight track without any assumption made on the prior position of the tracker. In global coordinates, on average, the track reconstructed between TOF1 and TOF2 should agree with the track reconstructed in either tracker, i.e. the mean residuals should be zero. Applying this reasoning to the unknown offset and angles yields to a system of equations for the four unknown constants [21]. The measurement of four residual distributions per tracker yields the alignment  
 375 constants. The main source of bias was the scattering in the material between TOF1 and TOF2. If the beam was not perfectly centred, particles preferentially scraped out on one side of the magnet bore, anisotropically truncating the tail of the residual distribution. The selection criteria defined above remove this effect.

Data was recorded with the superconducting magnets of the experiment turned off. High momentum beams were used to reduce the RMS scattering angle and maximise transmission. Each data set was processed independently.  
 380 Figure 18 shows the alignment parameters measured for each run during a specific ISIS user cycle. The measurements were in good agreement with one another and showed no significant discrepancy: an agreement between the independent fits guaranteed an unbiased measurement of the alignment constants. The constant fit  $\chi^2/\text{ndf}$  was close to unity for each fit, which indicated that there were no significant additional source of uncertainty. The optimal parameters are summarised in table 4.

	x [mm]	y [mm]	$\alpha$ [mrad]	$\beta$ [mrad]
TKU	$-0.032 \pm 0.094$	$-1.538 \pm 0.095$	$3.382 \pm 0.030$	$0.412 \pm 0.029$
TKD	$-2.958 \pm 0.095$	$2.921 \pm 0.096$	$-0.036 \pm 0.030$	$1.333 \pm 0.030$

Table 4: Summary table of the optimal alignment constants measured in the high-momentum straight-track data acquired during the 2017/01 ISIS user cycle.

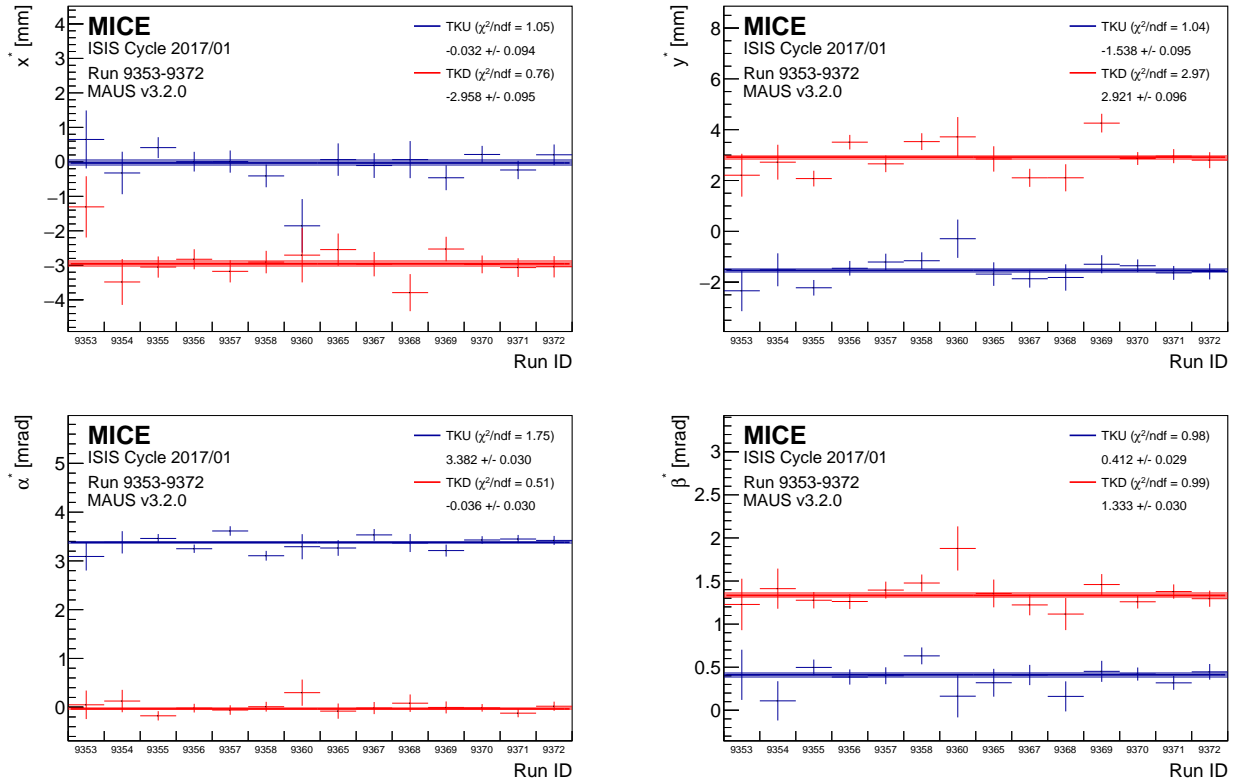


Figure 18: Consistency of the alignment algorithm across runs acquired during the 2017/01 ISIS user cycle.

## 385 9 Liquid-Hydrogen Absorber

### 9.1 Introduction

The absorber vessel comprise a cylindrical aluminium body sealed with two thin aluminium end windows, as shown in figure 19. The absorber vessel was specified to contains 221 of liquid, so the body had an inner diameter of 300 mm and a length between its end flanges of 230 mm. The length along the central axis between the two domes of the thin aluminium end windows was 350 mm [22].

### 9.2 Systematic studies

#### 9.2.1 Variation of the density of liquid-hydrogen due to varying temperature and pressure

The energy lost by a muon travelling through the liquid-hydrogen absorber depends on the path length the muon travelled through and on the density of the liquid-hydrogen. The density of liquid-hydrogen is a function of temperature and pressure. The temperature of the vessel was recorded by eight LakeShore Cernox 1050 SD

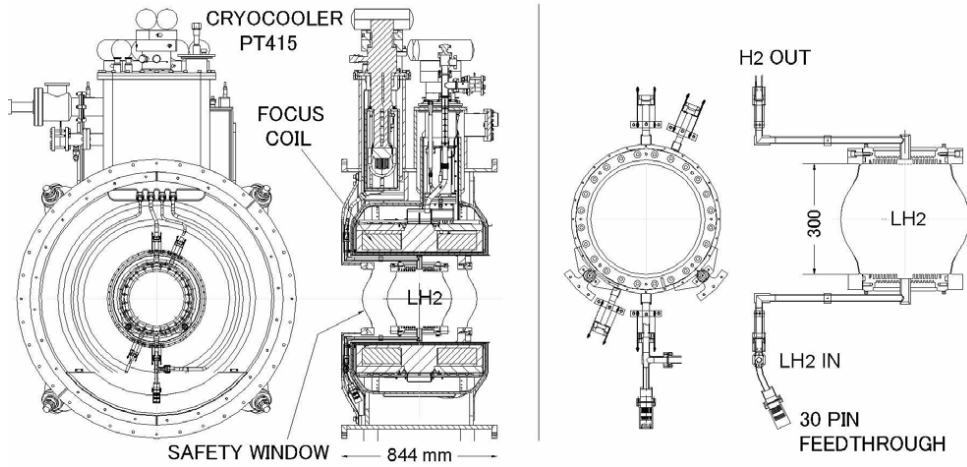


Figure 19: Left panel: Drawing of the absorber/focus-coil (AFC) module showing the principal components. Right panel: detail of the liquid-hydrogen absorber vessel.

sensors with a resolution of 0.1 K. Four of the sensors were used solely as temperature sensors, while the other four were used also as level sensors to ensure the liquid-hydrogen reached the top of the vessel. They were arranged in pairs with two mechanically clamped at the top of the vessel, two at a rotation of 45°, a further two at a further rotation of 90° and a final two at a further rotation of 45° to be at the bottom of the vessel.

400 cooldown and liquefaction were completed slowly over eight days at a pressure of 1.15 Bar after which the vessel's pressure was lowered to 1.085 Bar [22]. The vessel then remained in this steady-state equilibrium until the venting process began. During this process the cryocooler was switched off and the heaters were switched on, delivering a nominal power of 50 Watt to the absorber vessel. This resulted in an increase in pressure and temperature until the temperature stabilised at the boiling point. A rapid increase in temperature was observed  
405 once all the liquid-hydrogen had boiled off.

The sensors have a typical accuracy of  $\pm 9$  mK and a long-term stability of  $\pm 12$  mK at 20 K. The magnetic-field dependent temperature error at 2.5 T is 0.04%,  $\Delta T/T$ , equivalent to  $\pm 8$  mK at 20 K [23][24]. These are the quoted uncertainties given by the manufacturer of the sensors. The importance of magnetic fields on temperature measurements is that they cause reversible calibration shifts: when the magnetic field is removed,  
410 the sensors return to their original calibration.

To reduce the uncertainty in the liquid-hydrogen density a calibration procedure was devised using the boiling point: the corrected temperature reading was found by applying a cut-off correction, a magnetic field correction based on the focus coil current and mode, a correction for the non-linearity of the sensors, and a boiling point scaling factor [25].

415 The boiling point of hydrogen at 1.085 Bar is 20.511 K (figure 20). There are however a number of uncertainties. The sensors have a total uncertainty of 17 mK (9 mK accuracy, 12 mK stability, 8 mK magnetic). The non-linearity of the sensors adds 0.03 K. The temperature scaling and magnet current correction factors also have an associated error as they are based on the 0.1K resolution. For example, a calibrated sensor at boiling temperature and 1.505 Bar should read 21.692 K but can only read 21.65 K (21.6 K cut-off plus 0.05 cut-off  
420 correction) i.e. it is off by 0.042 K. The pressure sensors have an uncertainty of  $\pm 5$  mBar which equates to  $\pm 0.016$  K during steady state. The pressure uncertainty ( $\pm 5$  mBar) adds another uncertainty to the temperature calibration constants of  $\pm 0.014$  K. Collectively, all these uncertainties add up to 0.2 K for each sensor.

425 For our steady state condition the liquid-hydrogen was close to the boiling temperature of liquid parahydrogen [25]. The average temperature of the eight sensors during steady-state was  $(20.51 \pm 0.07)$  K at 1.085 Bar and allows us to determine the uncertainty in the density as  $(70.53 \pm 0.08)$  kg/m<sup>3</sup>

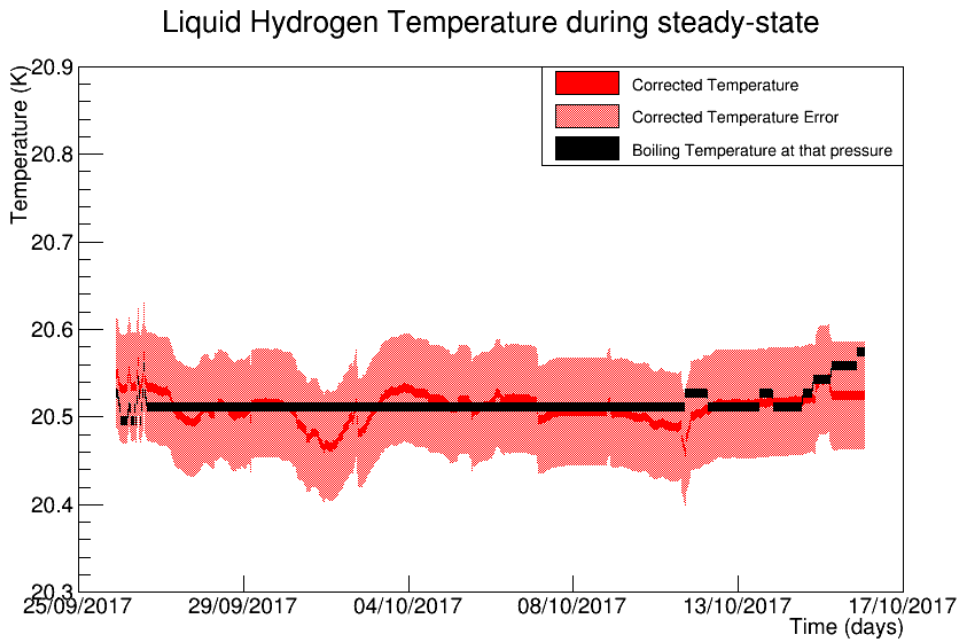


Figure 20: Average LH<sub>2</sub> temperature recorded by the sensors during the steady-state period. After applying all the correction factors the temperature remains at or close to the boiling point temperature.

### 9.2.2 Contraction of the absorber vessel due to cooling

The aluminium absorber vessel was cooled from room temperature to the operating temperature of the experiment (20.51 K), which resulted in the vessel contracting. The linear contraction of Al-6061 as it is cooled from 293K is given by:

$$\alpha = -4.1277 \times 10^{-3}T - 3.0389 \times 10^{-6}T^2 + 8.7696 \times 10^{-8}T^3 - 9.9821 \times 10^{-11}T^4 \quad (4)$$

where T is the operating temperature [26]. The equation is a line of best fit of data collated by NIST (National Institute of Standards and Technology) and has an associated curve fit error of 4%. At the MICE operating temperature, this corresponds to a linear contraction of the vessel along each plane of 0.415%, resulting in a warm bore length (350 mm) contraction of  $(1.45 \pm 0.05)$  mm. The vessel was held suspended in place, meaning the vessel was free to contract along each plane without restriction, since the vessel was free to contract within the warm bore of the focus coil.

### 9.2.3 Deflection of absorber vessel windows due to internal pressure

To minimise energy loss and Coulomb scattering by the absorber vessel, the windows were kept as thin as possible. They must however not rupture when handling any internal pressure they are subjected to. For safety considerations [22][27] it was necessary for the liquid-hydrogen circuit to be pressurised above atmospheric pressure to prevent air ingress. The vessel must also be capable of handling up to 1.5 Bar, the relief valve set pressure.

These pressures resulted in a deflection of the absorber windows and were modelled using ANSYS [28]. The uncertainty in the model's window deflection was 20%. It showed a linear expansion of the window deflection with pressure up to 2 Bar when the windows begin to yield. The pressure sensors were accurate to  $\pm 5$  mBar

445 (0.25% of 2 Bar). At  $(1085 \pm 5)$  mBar, the typical MICE operating pressure, this corresponded to a deflection of  $(0.5374 \pm 0.1076)$  mm (model uncertainty)  $\pm 0.0022$  mm (sensor uncertainty) at the centre of the absorber window.

### 9.2.4 Variation of the absorber vessel window thicknesses

450 The amount of energy loss and cooling experienced by a muon passing through the absorber depends on the amount of aluminium and liquid-hydrogen traversed. There were four windows, two absorber wall windows of the vessel and two safety windows.

455 At the centre of the absorber, the total amount of aluminium the muon beam passes through was  $(785 \pm 13)$   $\mu\text{m}$ , a variance of 1.68%. However, as the windows were thin, the effects on energy loss were negligible. A  $200\text{ MeV}/c$  muon passing along the central axis of an empty absorber loses  $0.345\text{ MeV}$ , which introduces a  $0.006\text{ MeV}$  uncertainty on energy loss.

### 9.2.5 Total Systematic Uncertainty on Energy Loss

In total there are three main contributions to the systematic uncertainty of the liquid-hydrogen absorber on energy loss. The contraction of the absorber and deflection of the absorber window due to internal pressure reduces the central warm bore length by  $(0.4 \pm 0.2)$  mm.

460 The combined absorber window's thickness variation at the centre of the absorber is  $13\text{ }\mu\text{m}$ . The average temperature during the steady state period of the experiment when the pressure remained constant at  $(1085 \pm 5)$  mBar is  $(20.51 \pm 0.07)$  K corresponding to a liquid-hydrogen density of  $(70.53 \pm 0.08)$  kg/m<sup>3</sup>.

465 The energy loss is momentum dependent as each particle will lose a different amount of energy passing through the absorber. Tables 5 and 6 show the energy loss at various momenta and densities of Aluminium and liquid-hydrogen [29][30][31][32].  $277\text{ MeV}/c$  and  $344\text{ MeV}/c$  are the minimum ionization momenta of Aluminium and liquid-hydrogen respectively.

Table 5: Energy Loss for Aluminium (Al-6061) at various momenta with a density of  $2.699\text{ g/cm}^3$ .

Momentum (MeV/c)	100	140	200	277
Mass Stopping Power (MeVg <sup>-1</sup> cm <sup>2</sup> )	1.798	1.688	1.630	1.615
Stopping Power (MeVcm <sup>-1</sup> )	4.8528	4.556	4.3994	4.3589

470 During the MICE experiment muon beam of momentum 140, 170, 200 and  $240\text{ MeV}/c$  were used. The energy loss and its uncertainty were calculated. The calculation used a central bore length of  $(349.6 \pm 0.2)$  mm, a total window thickness of  $(0.785 \pm 0.013)$  mm and a liquid-hydrogen density of  $(70.53 \pm 0.08)$  kg/m<sup>3</sup> for a particle travelling straight through the centre of the absorber.

475 For a  $140\text{ MeV}/c$  muon particle this corresponds to an energy loss of  $(10.88 \pm 0.02)$  MeV, while for a  $200\text{ MeV}/c$  muon particle this corresponds to an energy loss of  $(10.44 \pm 0.02)$  MeV. In terms of energy loss, the systematic error is 0.2%. This is for a particle travelling along the central axis of the absorber. A muon travelling through the absorber in the presence of a magnetic field would take a different path and thus would traverse a different length of aluminium and liquid-hydrogen.

Table 6: Energy loss for liquid-hydrogen at various densities (0.0703 to 0.0708 g/cm<sup>3</sup>) and various momenta of muons.

Momentum	100	140	200	344
Mass Stopping Power	4.568	4.267	4.104	4.034
Stopping Power (at $\rho=0.0703$ )	0.3211	0.29997	0.2885	0.28359
Stopping Power (at $\rho=0.07054$ )	0.3222	0.30099	0.2895	0.2846
Stopping Power (at $\rho=0.07078$ )	0.3233	0.3020	0.29048	0.2855
Stopping Power (at $\rho=0.0708$ )	0.3234	0.3021	0.29056	0.2856

## 10 Conclusions

A complete set of particle detector have permitted the full characterisation and study of the evolution of the phase space of a muon beam through a section of a cooling channel, leading to the first measurement of ionization cooling with unique level of precision and detail. All the different elements of the MICE instrumentation

480 have been used to characterise the beam and the measurement of the cooling performance for a different variety of beams momenta, emittance, and absorbers. Proving a technique critical for a muon collider and a neutrino factory brings those facilities a step closer.

## References

- [1] S. Geer, “Neutrino beams from muon storage rings: Characteristics and physics potential,” *Physical Review D* **57** no. 11, (Jun, 1998) 6989–6997, arXiv:hep-ph/9712290 [hep-ph].  
485
- [2] D. Neuffer, “Principles and Applications of Muon Cooling,” *Part. Accel.* **14** (1983) 75–90.
- [3] MICE Collaboration, M. Bogomilov *et al.*, “Demonstration of cooling by the Muon Ionization Cooling Experiment,” *Nature* **578** (2020) 53–59, arXiv:1907.08562 [physics.acc-ph].
- [4] M. Bonesini, “The design of MICE TOF0 detector,” *MICE Note 145* (2006) .  
490       <http://mice.iit.edu/micenotes/public/pdf/MICE0145/MICE0145.pdf>.
- [5] R. Bertoni *et al.*, “The construction and laboratory tests for MICE TOF0/1 detectors,” *MICE Note 241* (2008) . <http://mice.iit.edu/micenotes/public/pdf/MICE0241/MICE0241.pdf>.
- [6] R. Bertoni *et al.*, “The design and commissioning of the MICE upstream time-of-flight system,” *Nuclear Instruments and Methods in Physics Research A* **615** (Mar., 2010) 14–26, arXiv:1001.4426  
495       [physics.ins-det].
- [7] R. Bertoni *et al.*, “The construction of the MICE TOF2 detector,” *MICE Note 286* (2010) .  
     <http://mice.iit.edu/micenotes/public/pdf/MICE0286/MICE0286.pdf>.
- [8] D. Rajaram and V. C. Palladino, “The Status of MICE Step IV,”.  
     <http://accelconf.web.cern.ch/AccelConf/IPAC2015/papers/thpf122.pdf>.
- 500 [9] M. Bonesini, “Progress of the MICE experiment,” arXiv:1510.08825 [physics.acc-ph].
- [10] The MICE Collaboration, “Characterisation of the muon beams for the Muon Ionisation Cooling Experiment,” *ArXiv e-prints* (June, 2013) , arXiv:1306.1509 [physics.acc-ph].
- [11] D. Adams *et al.*, “Pion contamination in the MICE muon beam,” *Journal of Instrumentation* **11** (Mar., 2016) P03001, arXiv:1511.00556 [physics.ins-det].
- 505 [12] MICE Collaboration, M. Bogomilov *et al.*, “The MICE Muon Beam on ISIS and the beam-line instrumentation of the Muon Ionization Cooling Experiment,” *JINST* **7** (2012) P05009,  
     arXiv:1203.4089 [physics.acc-ph].
- [13] Y. Karadzhov *et al.*, “TOF detectors Time Calibration,” *MICE Note 251* (2009) .  
     <http://mice.iit.edu/micenotes/public/pdf/MICE0251/MICE0251.pdf>.
- 510 [14] L. Cremaldi *et al.*, “Progress on Cherenkov Reconstruction in MICE,” *MICE Note 473* (2015) .  
     <http://mice.iit.edu/micenotes/public/pdf/MICE0473/MICE0473.pdf>.
- [15] R. Asfandiyarov *et al.*, “The design and construction of the MICE Electron-Muon Ranger,” *Journal of Instrumentation* **11** (Oct., 2016) T10007, arXiv:1607.04955 [physics.ins-det].
- [16] F. Drielsma, “Electron-Muon Ranger: hardware characterization,” Master’s thesis, University of Geneva,  
515 2014. <https://arxiv.org/abs/1710.06946>.
- [17] D. Adams *et al.*, “Electron-muon ranger: performance in the MICE muon beam,” *Journal of Instrumentation* **10** (Dec., 2015) P12012, arXiv:1510.08306 [physics.ins-det].

- [18] F. Drielsma, *Measurement of the Increase in Phase Space Density of a Muon Beam through Ionization Cooling*. PhD thesis, University of Geneva, 10, 2018.
- 520 [19] M. Ellis *et al.*, “The Design, construction and performance of the MICE scintillating fibre trackers,” *Nucl. Instrum. Meth.* **A659** (2011) 136–153, 1005.3491.
- [20] **D0** Collaboration, V. M. Abazov *et al.*, “The Upgraded D0 detector,” *Nucl. Instrum. Meth.* **A565** (2006) 463–537, physics/0507191.
- 525 [21] F. Drielsma, “Beam-based detector alignment in the MICE muon beam line,” arXiv:1805.06623 [physics.ins-det]. <https://arxiv.org/abs/1805.06623>.
- [22] V. Bayliss *et al.*, “The liquid-hydrogen absorber for mice,” *Journal of Instrumentation* **13** no. 09, (2018) T09008. <http://stacks.iop.org/1748-0221/13/i=09/a=T09008>.
- [23] “Cernox RTDs [Accessed 2 Oct. 2018],”.  
[https://www.lakeshore.com/Documents/LSTC\\_Cernox\\_1.pdf](https://www.lakeshore.com/Documents/LSTC_Cernox_1.pdf).
- 530 [24] “Temperature Measurement and Control Catalog [Accessed 2 Oct. 2018],”.  
[https://www.lakeshore.com/Documents/LakeShoreTC\\_1.pdf](https://www.lakeshore.com/Documents/LakeShoreTC_1.pdf).
- [25] C. Brown *et al.*, “Systematic Uncertainties in the LH2 absorber,” *MICE Note 524* (2018).  
<http://mice.iit.edu/micenotes/public/pdf/MICE0524/MICE0524.pdf>.
- [26] G. Hardin, “Aluminum 6061-T6 (UNS AA96061) [Accessed 3 Oct. 2018],”.  
<https://www.nist.gov/mml/acmd/aluminum-6061-t6-uns-aa96061>.
- 535 [27] S. Ishimoto *et al.*, “Liquid Hydrogen Absorber for MICE,” *Conf. Proc. C100523* (2010) 421–423.
- [28] M. Green *et al.*, “Does One Know the Properties of a MICE Solid or Liquid Absorber to Better than 0.3 Percent?,” *MICE Note 155* (2006).  
<http://mice.iit.edu/micenotes/public/pdf/MICE0155/MICE0155.pdf>.
- 540 [29] “Atomic and nuclear properties of Aluminium,”.  
[http://pdg.lbl.gov/2017/AtomicNuclearProperties/HTML/aluminum\\_Al.html](http://pdg.lbl.gov/2017/AtomicNuclearProperties/HTML/aluminum_Al.html).
- [30] “Atomic and nuclear properties of liquid Hydrogen,”. [http://pdg.lbl.gov/2017/AtomicNuclearProperties/HTML/liquid\\_hydrogen.html](http://pdg.lbl.gov/2017/AtomicNuclearProperties/HTML/liquid_hydrogen.html).
- [31] “Muon in Aluminium,”. [http://pdg.lbl.gov/2017/AtomicNuclearProperties/MUE/muE\\_aluminum\\_Al.pdf](http://pdg.lbl.gov/2017/AtomicNuclearProperties/MUE/muE_aluminum_Al.pdf).
- 545 [32] “Muons in liquid Hydrogen,”. [http://pdg.lbl.gov/2017/AtomicNuclearProperties/MUE/muE\\_liquid\\_hydrogen.pdf](http://pdg.lbl.gov/2017/AtomicNuclearProperties/MUE/muE_liquid_hydrogen.pdf).